A multimodal imaging study to highlight elastin-derived peptide pro-tumoral effect in a pancreatic xenograft model

Lise Nannan, Willy Gsell, Sarah Belderbos, Célia Gallet, Jens Wouters, Sylvie Brassart-Pasco, Uwe Himmelreich, Bertrand Brassart

Title: A multimodal imaging study to highlight elastin-derived peptide pro-tumoral effect in a pancreatic xenograft model

Authors:

Lise Nannan[1,2,3], Willy Gsell[1], Sarah Belderbos[1], Célia Gallet[2,3], Jens Wouters[1], Sylvie Brassart-Pasco[2,3], Uwe Himmelreich[1#], Bertrand Brassart[2,3#*]

Affiliations:

1-KU Leuven, Department of Imaging and Pathology / Biomedical MRI, Leuven, Belgium

2-CNRS UMR 7369 Matrice Extracellulaire et Dynamique Cellulaire, Reims, France

3- Université de Reims Champagne Ardenne, Laboratoire de Biochimie Médicale et Biologie Moléculaire, Reims, France.

co-last authors

***: Corresponding author:**

Dr. B. BRASSART, Laboratoire de Biochimie Médicale et de Biologie Moléculaire, UMR CNRS / URCA 7369 MEDyC, UFR Médecine, 51 Rue Cognacq Jay, 51095, Reims Cedex, France.

Phone : 33.3.26.91.80.56; Fax : 33.3.26.91.80.55; Email : bertrand.brassart@univ-reims.fr

https://orcid.org/0000-0002-4879-6832

Abstract:

Background

Pancreatic ductal adenocarcinoma (PDAC) is highly malignant with a very poor prognosis due to its silent development and metastatic profile with a 5-year survival rate below 10%. PDAC is characterized by an abundant desmoplastic stroma modulation that influences cancer development by extracellular matrix/cell interactions. Elastin is a key element of the extracellular matrix. Elastin degradation products (EDPs) regulate numerous biological processes such as cell proliferation, migration and invasion. The aim of the present study was to characterize for the first time the effect of two EDPs with consensus sequences "GxxPG" and "GxPGxGxG" (VG-6 and AG-9) on PDAC development. VGVAPG (VG-6) and AGVPGLGVG (AG-9) on PDAC development. The ribosomal protein SA (RPSA) has been discovered recently, acting as a new receptor of EDPs on the surface of tumor cells, contributing to poor prognosis.

Methods

Six week-old female Swiss nude *nu/nu* (Nu(Ico)-*Foxn1*^{nu}) mice were subcutaneously injected with human PDAC MIA PaCa-2/eGFP-FLuc^{+} cells, transduced with a purpose-made lentiviral vector, encoding green fluorescent protein (GFP) and *Photinus pyralis* (firefly) luciferase (FLuc). Animals were treated three times per week with AG-9 (n=4), VG-6 (n=5) or PBS (n=5). The influence of EDP on PDAC was examined by multimodal imaging (bioluminescence imaging (BLI), fluorescence imaging (FLI) and magnetic resonance imaging (MRI). Tumor volumes were also measured using a caliper. Finally, immunohistology was performed at the end of the *in vivo* study.

Results

After *in vitro* validation of MIA PaCa-2 cells by optical imaging, we demonstrated that EDPs exacerbate tumor growth in the PDAC mouse model. While VG-6 stimulated tumor growth to some extent, AG-9 had greater impact on tumor growth. We showed that the expression of the RPSA correlates with a possible effect of EDPs in the PDAC model. Multimodal imaging allowed for longitudinal *in vivo* follow-up of tumor development. In all groups, we showed mature vessels ending in close vicinity of the tumor, except for the AG-9 group where mature vessels are penetrating the tumor reflecting an increase of vascularization.

Conclusions

Our results suggest that AG-9 strongly increases PDAC progression through an increase in tumor vascularization.

Keywords: Pancreatic ductal adenocarcinoma, multimodal imaging, *in vivo*, elastin-derived peptides, cancer progression.

INTRODUCTION

Pancreatic ductal adenocarcinoma (PDAC) is the most frequent pancreatic malignancy (90% of pancreatic cancers). It is expected to become the second leading cause of cancer-related death by 2030 (1). The poor prognosis is mainly due to late diagnosis and high invasiveness with dissemination of metastases in the advanced stage of the disease. Gold standard treatments consist of surgical resection; chemotherapy or combined radio- and chemotherapy (e.g., gemcitabine and 5-fluorouracile). However, all therapies have a limited responsiveness (2). The 5-year survival rate remains below 10% (3). Consequently, alternative therapeutic approaches are of critical need, with the identification of biomarkers allowing early detection of PDAC, together with the development of new tools for clinical imaging. The microenvironment of PDAC is complex and is composed of two entities: the PDAC cells themselves and the stroma composed of cancer-associated fibroblasts, pancreatic stellate cells, endothelial cells, immune cells, various growth factors/cytokines and an abundant extracellular matrix (ECM) (4).

PDAC is histologically characterized by the abundance of extracellular matrix (ECM) components, also referred to as desmoplasia. ECM components have been highlighted as a major contributor to PDAC progression and to resistance to therapy (5,6). ECM components include collagens, elastin, proteoglycans as well as ECM remodeling enzymes involved in degradation or cross-linking of the ECM components. Elastin is a fibrous protein of the ECM, responsible for the structural integrity and function of tissues. This protein is extremely stable, resistant and its half-life is estimated to be approximately 70 years (7). During physiological (8,9) or pathological conditions (10,11), elastin is degraded by elastases that release elastin-derived peptides (EDPs). Pancreatic elastase, which has been discovered by Baló and Banga, accumulates near the degradation site (12). Other proteases have been described, such as serine proteases, cysteine proteases and matrix metalloproteinases (MMPs) (8). Also called matrikines, the released EDPs with a consensus sequence “GXXPG” or “GxPGxGxG” have biological activities (13). In cancer, EDPs, especially VGVAPG (VG-6) and AGVPGLGVG (AG-9) peptides, favor tumor progression and metastasis formation by increasing MMP-2, MMP-9 MT1-MMP, uPA and Hsp90 secretion (14–16). VG-6 and AG-9 peptides are located within exons 24 and 26 of human tropoelastin, respectively. RPSA, a 37-67 kDa protein, interacts with several ECM proteins such as laminin-1 and EDPs (17–19), including AG-9 peptide. RPSA regulates biological processes such as cell differentiation, adhesion and migration through induction of signaling transduction pathways (20). This is also a membrane receptor for pathogens, prions and growth factors. Moreover, RPSA is involved in the assembly and/or stability of the 40S ribosomal subunit. Recently, Lefebvre *et al.* suggested that the transient receptor potential melastatin-related 7 (TRPM7) channel/RPSA complex could regulate human pancreatic cancer cell migration (21).

It is our hypothesis that EDPs which accumulate in PDAC stroma, especially AG-9 and VG-6 peptides, may promote tumor growth. We first decided to assess the overexpression of RPSA in PDAC tissue based on literature data. We then selected a subcutaneous PDAC model to study AG-9 and VG-6 effects on tumor growth using different methodologies (caliper, MRI, BLI and FLI). This model presents several advantages, which include technical feasibility and tumor accessibility (direct measurement of the subcutaneous tumor), allowing longitudinal follow up. In the context of translational research, different non-invasive imaging techniques have been tested and further developed allowing diagnosis, staging and longitudinal evaluation for preclinical and clinical purposes. Currently, PDAC diagnosis mainly relies on tissue sample analysis and medical imaging, namely computed tomography (CT), magnetic resonance imaging (MRI) and endoscopic ultrasound guided fine-needle aspiration (22–26). From a preclinical point of view, optical imaging is another widely used method. It includes bioluminescence imaging (BLI) and fluorescence imaging (FLI). BLI is based on the detection of photons resulting in D-luciferin degradation by luciferase (e.g., the *Photinus pyralis* (firefly) luciferase (FLuc)), which is expressed by genetically modified cells. FLI is based on the detection of fluorescent proteins, allowing longitudinal non-invasive follow up of tumor growth in individual animals (27,28). These techniques provide valuable information on cell viability, cell density and expression of targeted genes with longitudinal profiles on temporal and spatial distribution. However, they are restricted to preclinical use due to limitations (e.g., poor depth penetration of light, need for cell engineering to express the imaging genes, poor resolution, etc.), preventing its direct translation to clinical use. MRI is a preclinical and clinical imaging technique with high spatial resolution and good soft tissue contrast enabling determination of tumor location and size. It provides an excellent soft tissue contrast with multi-parametric, quantitative read-outs (T_1- and T_2-weighted, proton density, water diffusion, perfusion, metabolism, function and vascularization) with no need of ionizing radiation as opposed to CT (29,30). Multimodal imaging allows to maximize the amount of molecular, functional, anatomical and metabolic information on the same subject over time. It is a powerful approach to improve the understanding of tumor growth and to accelerate the discovery of new therapeutic strategies for cancer.

MATERIALS AND METHODS

Bioinformatics and clinical data mining

The pattern of RPSA expression and staining in human clinical samples was characterized using the Human Protein Atlas web portal (available from www.proteinatlas.org). Semi-quantitative analysis was performed from 10 pancreatic cancer cases for classification of immunohistochemical (IHC) outcome (staining intensity and fraction of stained cells).

Elastin-Derived Peptides

The elastin-derived nonapeptide AG-9 (AGVPGLGVG), hexapeptide VG-6 (VGVAPG), TAMRA-AG-9 and TAMRA-VG-6 were synthesized and purified by ProteoGenix.

Cell Culture

The human ductal pancreatic adenocarcinoma MIA PaCa-2/WT cell line was obtained from the American Type Culture Collection (ATCC® CRL-1420). The cells were cultured in DMEM (Gibco) containing 4.5g/L glucose supplemented with 10% FBS (Sigma-Aldrich) and 1% penicillin-streptomycin antibiotics (Gibco). Flasks were kept at +37°C in an incubator with controlled 5% CO_2. The absence of mycoplasma was controlled.

Cell Transduction

An HIV-based viral vector (pCH-EF1a-eGFP-T2A-FLuc-IRES-PuroR) was generated by the Leuven Viral Vector Core (KU Leuven) as described before (31). MIA PaCa-2/WT cells were seeded on plates and were transduced with lentiviral vectors (10 vectors per cell) during 24h incubation. MIA PaCa-2-transduced cells (MIA PaCa-2/eGFP-FLuc$^+$) were selected by supplementing the growth medium with 10µg/mL puromycin (Merck Millipore) over a time period of two weeks.

Immunocytochemistry

Cells were seeded on glass coverslips and incubated in DMEM supplemented by 10% FBS for 24h at a temperature of +37°C in the presence or absence of EDPs, TAMRA AG-9 and TAMRA VG-6. After washing, cells were incubated with an anti-RPSA antibody (Abcam, ab137338) in culture medium supplemented with 1% (BSA), washed and incubated with the AlexaFluor™ 405 goat anti-rabbit secondary antibody (Thermo Fisher Scientific, A31556). Cells were fixed with 4% paraformaldehyde (PFA, Electron Microscopy Sciences) solution. Coverslips were mounted and fixed on the slide with a mounting solution containing DAPI (Thermo Fisher Scientific). Immunofluorescence-labeled cell preparations were imaged using a Zeiss LSM710® NLO confocal laser scanning microscope (Carl ZEISS SAS) with the 63x oil-immersion objective (ON1.4) coupled with a CHAMELEON femtosecond Titanium-Sapphire Laser (Coherent). GFP and TAMRA were sequentially excited at 488nm of Argon laser and diode laser 561nm. Emitted signals were respectively collected with 493-560nm and 570-700 bandpass filters. Alexa405 was collected by using 740nm excitation wavelength with 420–440 bandpass filters. Image acquisitions were performed with ZEN Software (Carl ZEISS SAS). All acquisition settings were constant between specimens.

Western Blotting analysis

Western-blot analyses were performed as previously described (Brassart *et al*, 2019). The mouse anti-GFP (MA5-15256), rabbit anti-FLuc (ab21176) and horseradish peroxidase-conjugated secondary anti-

IgG antibody (goat anti-mouse IgG (H + L) and goat anti-rabbit IgG (H + L) (NA931V and NA934V)) were purchased from Thermo Fisher Scientific, Abcam and GE Healthcare, respectively.

RNA Isolation and Real-Time PCR Analysis

Total RNA was isolated from MIA PaCa-2/WT and MIA PaCa-2/eGFP-FLuc^{+} cells using the RNeasy Plus Mini kit (Qiagen) following the manufacturer's instruction. The amount and integrity of isolated RNA were analyzed using the Bioanalyzer RNA 6000 nano assay (Agilent Technologies). Single-stranded cDNA was synthesized using a maxima first strand cDNA synthesis kit for RT-qPCR (Thermo Scientific). Real-Time PCR was performed using the maxima SYBR Green/ROX qPCR Master Mix (Thermo Scientific) according to the manufacturer's instructions, the thermocycler Agilent MX300P device and the MxPro software (Agilent Technologies). Relative expression of different gene transcripts was calculated using the ΔCt method. The Ct of the gene of interest was normalized to the Ct of the normalizer (EEF1A1).

RT-qPCR primers were designed according to the sequence of RPSA (NM_002295). The forward primer for RPSA was 5'-CCA-TTG-AAA-ACC-CTG-CTG-AT-3' and the reverse primer was 5'-CTG-CCT-GGA-TCT-GGT-TAG-TGA-3' with a 144bp product. The forward primer for EEF1a1 was 5'-CTG-GAG-CCA-AGT-GCT-AAC-ATG-CC-3' and the reverse primer was 5'-CCG-GGT-TTG-AGA-ACA-CCA-GTC-3' with a 221bp product. All primers were synthesized by Eurofins.

***In vivo* experiments**

The in vivo experiments were conducted according to European regulations on the protection of animals used for scientific purposes (Directive 2010/63/EU) and their Belgian (Royal Decree of 29 May 2013) and Flemish implementations (Decision of the Flemish Government to adapt the Royal Decree of 29 May 2013, 17 February 2017) on principles for laboratory animal care. The experimental *in vivo* procedures were approved by the Animal Ethics Committee of KU Leuven (ECD p259/2015). Based on previous data of an *in vivo* melanoma model (16), power calculations for the required animal numbers were made resulting in a sample size of n=5 to demonstrate a significant effect of EDPs. As shown in figure S1, all groups started with 5 animals. Unfortunately, no tumor development was observed in one mouse of the AG9 group and two mice died (control and VG-6 groups) during the last imaging session. Six week old female Swiss Nude *nu/nu* (Nu(Ico)-*Foxn1*^{nu}) mice (average body weight, 20-24g) were purchased from Charles River Laboratories. Animals were housed at the animal facility of KU Leuven in standard, individually ventilated cages under a 12h light/dark cycle under controlled environmental conditions of humidity (50-70%) and temperature (22±2°C) with food and water supplied *ad libitum*. Animal cages were kept in a room with constant temperature and humidity. All mice were acclimatized to our laboratory conditions for one week before starting the experiments. For induction of the tumor model and imaging, mice were anesthetized using 2% isoflurane (IsoVET, 100 mg/g, Eurovet, Piramal, Healthcare) in 100% oxygen. Mice were sacrificed at the end of the experiments.

Murine xenograft model

For the subcutaneous (s.c.) PDAC model, 3.5 10^6 MIA PaCa-2/eGFP-FLuc$^+$ cells suspended in 100µL of sterile DPBS were implanted subcutaneously into the right flank of randomized groups of Swiss Nude nu/nu (Nu(Ico)-*Foxn1*^{nu}) mice (Charles River Laboratories). MIA PaCa-2/eGFP-FLuc$^+$ cells were preincubated for 30min in sterile PBS (control; *n*=5; Gibco), AG-9 (*n*=5) or VG-6 (*n*=5) before the initial injection. Elastin-derived peptides were solubilized extemporaneously in sterile PBS (Gibco) to reach a final concentration of 10 mg/kg (mouse weight) for intraperitoneal injection. Intraperitoneal administrations of AG-9, VG-6 or control were performed three times per week during all experiments starting from tumor cell inoculation. Tumor volumes were determined using a caliper according to the following formulae: $v=(AxB^2)/2$, where A is the largest dimension of the tumor and B is the smallest dimension. Tumor measurements were performed three times per week. Animals were scanned at weeks 2, 3 and 4 using optical imaging to study cell viability by using BLI (FLuc) and the expression of eGFP in cell line by using FLI. At weeks 2 and 4, animals underwent MRI scans to study three-dimensional (3D) tumor volumes, tumor tissue heterogeneity and vascularization, using two-dimensional (2D) and 3D T_2-weighted MR images, MR angiography (MRA) and parametric maps (T_2-relaxation and apparent diffusion coefficients (ADC)). At the end of the study, mice were sacrificed, and tumors were surgically extracted, weighted, analyzed by *ex vivo* bioluminescence and then fixed in 4% PFA for histology studies (**figure S1**).

Bioluminescence Imaging

In vitro, *in vivo* and *ex vivo* BLI were performed using an IVIS Spectrum imaging system (Perkin Elmer). BLI was performed for estimating the number of viable, FLuc expressing cells. For *in vitro* experiments, MIA PaCa-2/WT and MIA PaCa-2/eGFP-FLuc$^+$ cells were seeded in quadruplicate on 48-well plate before imaging. An equal volume of D-luciferin solution (Luciferin-EF) was added. The signal was correlated with the number of cells present in each well by calculating the total photon flux (p/sec/cm²/sr). Regions of interest (ROIs) were placed over each well for quantification of the total photon flux using the Living Image software, version 4.2 (Perkin Elmer). For *in vivo,* experiments, mice were anesthetized with 2.5% isoflurane in 100% O_2 (2L/min) and placed in the imaging chamber of the IVIS Spectrum. A D-luciferin solution was injected intraperitoneally at a dose of 126 mg/kg body weight 10 min before imaging. For *ex vivo* imaging, a D-luciferin solution as for *in vivo* imaging was injected 10min before sacrifice. Then, the tumors were excised and placed in a D-luciferin solution. The BLI signal was acquired using the following settings: exposure time of 1second (for *in vivo* and *ex vivo*) or 10seconds (for *in vitro*) per image, F/stop of 1, a subject height of 1.5 cm, field-of-view of 22.8 cm and medium binning. The maximal radiance (p/s/cm²/sr) was then reported. Individual and identical ellipsoid ROIs of 5.8 cm² were placed over each tumor for quantification of the total photon flux.

Fluorescence Imaging

In vitro and *in vivo* FLI was performed using an IVIS Spectrum imaging system (Perkin Elmer). FLI was performed to estimate the protein transcription level of eGFP. *In vitro* experiments were performed on the same sample that was used for *in vitro* BLI. The FLI signal was acquired using the following settings: exposure time of 1second (for *in vivo*) or 4seconds (for *in vitro*) per image, F/stop of 1, a subject height of 1.5 cm, field-of-view of 22.8 cm and medium binning. The maximal radiance (p/s/cm²/sr) of the tumors was measured *in vitro* and *in vivo*. Individual and identical ellipsoid ROIs of 5.8 cm² were placed over each tumor for quantification of the total photon flux.

Small-Animal Magnetic Resonance Imaging

MRI measurements were acquired using a 7T Bruker Biospec small animal MR scanner (Bruker Biospin) with a horizontal bore of 30cm and equipped with actively shielded gradients ($200 mT.m^{-1}$). *In vivo* images were acquired using a quadrature radio-frequency resonator (transmit/receive; inner diameter 8.6 cm, Bruker Biospin). Body temperature and breathing rate of the animals were monitored using a physiological monitoring system (Small Animal Instruments Inc., Stony Brook) and maintained at 37±2˚C and 60-80min^{-1}, respectively. Animals were anesthetized and kept under anesthesia using 2.5% of isoflurane in 100% O_2. After obtaining initial localizer images, the protocol consisted of the acquisition of T_2-weighted anatomical reference images using a high-resolution 2D Turbo Rapid acquisition with relaxation enhancement (Turbo-RARE) sequence followed by a 3D T_2-weighted MR image using respiration gated acquisitions. To visualize if mature vessels are present within the tumor, we used a 3D MR angiography (time of flight) protocol. Tissue integrity (water content and cellular density) was investigated by acquisition of parametric T_2 maps (multi-slice multi-echo sequence) and apparent diffusion coefficient maps (diffusion MRI with EPI readout). MRI sequences and scan parameters are represented in **table S1**.

Histology

Harvested tumors were collected and fixed in PFA and stored in 0.1% sodium azide in PBS (Acros Organics) until further processing. Samples were transferred into a 15% sucrose solution in PBS at +4°C overnight and subsequently into a 30% sucrose solution in PBS before embedded with optimum cutting temperature compound (OCT, Thermo Fisher Scientific). Ten-micrometer sections were made using a cryostat-sectioning apparatus (NX70 Cryostat, Thermo Fisher Scientific). Histological analyses were performed on hematoxylin and eosin (HE) sections that were prepared by using routine histological methods. For IHC, sections were thawed, fixed in acetic acid, and dried at RT. Serum blocking was carried out with nonspecific binding immunoglobulin in 2% FBS, 10% donkey serum in PBS-Tween-20 0.5% (Sigma-Aldrich). Sections were incubated overnight with rabbit anti-RPSA antibody (Abcam, ab99484) and Firefly Luciferase (Abcam, ab21176). After washing with PBS, secondary the antibody was added for 90min at RT with the appropriated Alexa Fluor®647 conjugated donkey antibody (Abcam, ab150075) against rabbit IgG. After washing with PBS, the sections were counterstained with

DAPI-mounting medium (Thermo Fisher Scientific). All images were obtained with a Zeiss Axioscan Z.1 slide scanner microscope (Carl Zeiss) equipped with a Hamamatsu Orca Flash 4.0 V3 camera in combination with a Plan Apo 20x lens with a numerical aperture (NA) of 0.80. Alexa Fluor®647, GFP and DAPI were excited with red (640nm), green (561nm) and blue (488nm) diodes (100mW) and detected with BP538-562/BS570/BP570-640 (dsRed), BP450-490/BS495/BP500-550 (GFP) and BP335-383/BS395/BP420-470 (DAPI) emission filters, respectively. Images were then digitized using ZEN black (ZEN 3.2 version, Carl Zeiss Microscopy GmbH).

Statistical analysis

A stringent non-parametric statistical test, which does not preclude to have a Gaussian distribution of the data was performed. GraphPad Prism 8.2 software (GraphPad) was used for all statistical analyses. Data is expressed as the mean±SEM, SD or Min to Max. A *Mann-Whitney U* test was used for experiments. For all tests, statistical significance was assumed when $p<0.05$ (*, $ and #) and $p<0.01$ (**).

RESULTS

Justification for the choice of pancreatic tumor model.

The Human Protein Atlas presents an overview of protein and RNA expression in human tissue. The RPSA is present in most human organs except for skeletal muscle and adipose tissue (**Fig. 1a**). In the pancreas, RPSA is highly expressed. RPSA RNA is found in all human tissue (**Fig. 1b**). However, in lymph nodes and in the pancreas, the RPSA RNA level is higher than in other organs with 300.2 NX and 246.7 NX, respectively. RPSA immunohistochemistry (IHC) shows a strong staining in healthy pancreas tissue and differential protein expression ranging from weak to strong within pancreatic tumor tissue (**Fig. 1c-d**). In most cases, more than 75% of tumor cells are RPSA positive (**Fig. 1d**). During PDAC development, elastases release EDPs that were previously reported to favor tumor growth when they interact with RPSA (Da Silva *et al*, 2018). The high expression of RPSA in pancreatic tissue may contribute during the initial phase and/or to progression and aggressiveness of pancreatic cancer (32). Therefore, we decided to study the EDP effect *in vivo* in the PDAC model.

In vitro validation of engineered MIA PaCa-2 cells for optical imaging.

The MIA PaCa-2 pancreatic cell line was transduced to enable tumor monitoring by using optical imaging as described before (31). For this purpose, a lentiviral vector, encoding fluorescent eGFP and bioluminescent FLuc proteins, was used. The transduced MIA PaCa-2 cells were named MIA PaCa-2/eGFP-FLuc$^+$ (**Fig. 2a**). Successful insertion of the FLuc gene into cells was confirmed by *in vitro* BLI, as shown in **fig. 2b-c**. Hereby, different cell numbers ($1.25x10^4$-$1.00x10^5$) were analyzed. The *in vitro* BLI signal increased significantly in a cell number-dependent manner (*****$p>0.0286$). No signal was observed in the parental MIA PaCa-2 cells. In addition, successful transduction of the eGFP gene into

cells was confirmed by *in vitro* FLI, as shown in **fig. 2d-e**. The FLI signal in MIA PaCa-2/eGFP-FLuc$^+$ cells increased proportionally with increasing numbers of cells (*****p>0.0286). Furthermore, transduction of the FLuc and eGFP genes into cells was confirmed by western blotting on total protein extracts (**Fig. 2f**). The gene expression of RPSA was studied by RT-qPCR and revealed that in both cell lines the expression of RPSA was the same (**Fig. 2g**). Finally, colocalization of RPSA with TAMRA-AG-9 and TAMRA-VG-6 was evidenced in both cell lines (**Fig. 2h**). These results confirm that the new MIA PaCa-2/eGFP-FLuc$^+$ cell line is suitable for fluorescent and bioluminescent analysis. The expression of RPSA and the fixation of EDPs are not impacted by cell transduction.

Elastin-derived peptides boost tumor growth in a human pancreatic cancer mouse model.

We tested the effect of EDP on tumor growth in the xenograft pancreatic cancer model described in the Materials and Methods section. First, intraperitoneal administrations of EDP did not exhibit any other clinical sign or weight loss (**Fig. 3a**). For follow-up of tumor growth, tumors were measured every 2-3 days until day 28 (sacrifice). MIA PaCa-2/eGFP-FLuc$^+$ s.c. xenografts treated by AG-9 significantly accelerated tumor growth from day 14 to day 28 (**Fig. 3b**). At days 14 (*****p<0.0159), 16 (******p<0.0079), 19 (******p<0.0079), 21 (ns p<0.2063) and 28 (ns p<0.0.0794), tumor growth increased by two-fold compared to the control group. Moreover, MIA PaCa-2/eGFP-FLuc$^+$ s.c. xenografts treated by VG-6 show less tumor growth than AG-9 from day 16 (#p<0.0397) to day 28. *Ex vivo* evaluation after dissections shows that AG-9 treatment increased the tumor size by 2.3-fold and VG-6 treatment by 1.8-fold compared to controls. Weighting of surgically removed tumors confirmed this increase (2.41-fold) (**Fig. 3c-e**). Interestingly, this data also shows differences between VG-6 and the control group in terms of tumor size (increase by 1.64-fold) and weight (increase by 1.45-fold), suggesting a difference in tumor cell density. The same trend was observed between both EDPs when we compared AG-9 to VG-6 with 1.39-fold and 1.65-fold increases for tumor size and weight, respectively. To study further the impact of EDP on PDAC tumors, tumor sections were stained with HE (**Fig. 3f**). Tumors were homogeneous and solid masses of cells without necrotic areas. As tumors were reactive to the AG-9 peptide, the presence of its receptor has been investigated. Histological analysis shows the presence of RPSA in tumors (**Fig. 3g**). RPSA is also largely involved in tumor development.

Optical imaging confirmed the impact of Elastin-derived Peptides on tumor cells.

To further evaluate the effects of EDPs, we performed *in vivo* longitudinal BLI scans to assess the amount of viable cancer cells within the tumor tissue (**Fig. 4a-b**).

BLI results indicated a significant increase in signal intensity of tumors in the presence or after pre-incubation with AG-9 (increase of 3.0, 1.94 and 2.1-fold after week 2 (*****p<0.0159), 3 (*****p<0.0317) and 4 (*****p<0.0286), respectively). Concerning the impact of VG-6, the number of photons emitted from

tumors did not increase significantly but a trend of increased signal intensity was observed at all experimental time points (on average by 1.4-fold).

In vivo FLI was used for quantification of the signal intensity from tumor cells expressing eGFP (**Fig. 4c-d**). As for BLI measurements, we observed a significant increase in signal intensity (11.9-fold) when tumors were treated with AG-9 compared to the control group (*****p<0.0286). A 10-fold increase was observed when tumors were treated with VG-6 (*p<0.0159).

Ex vivo BLI analysis of isolated tumors showed an association between signal intensity (p/sec) and a high rank of tumor cell viability (**Fig. 4e-f**). The signal in AG-9 treated tumors at week 4 increased by 1.5-fold compared to control tumors. A similar trend was observed for VG-6 with a 1.24-fold increase compared to control tumors. Optical imaging and especially *in vivo* BLI showed that treatment with EDPs increased tumor development in terms of number of viable tumor cells. Like BLI, FLI shows differences in tumor growth by different signal intensities from the tumor regions. But, FLI appears less sensitive. Comparing both EDPs, AG-9 exerts a greater effect on pancreatic cancer development compared to VG-6. Histological analysis of FLuc and eGFP was performed to assess the presence of MIA-PaCa-2/eGFP-FLuc$^+$ cells. Presence of tumor cells was confirmed for lesions of all groups (**Fig. 4g-h**).

Magnetic resonance imaging based assessment of the impact of elastin-derived peptides on tumor growth.

Similar, to what was found with optical imaging, tumor volumes determined by anatomical T_2-weighted MRI) were higher in AG-9 (*****p<0.0357) compared to the control group (**Fig. 5a-b**) at week 2. At week 4, we showed the same effects on tumor volumes with AG-9 EDP (*****p<0.0286). Tumor volumes in the control group were lower than in the two other groups (201.4±56.7, 517±189 and 318.6±118.2mm^3 for control, AG-9 and VG-6 respectively, **table S2**). All tumors showed homogenous contrast on the 3D T_2w-RARE MR images with no sign of fluid cavities. Only a small hypointense region is visible in all tumors (blood vessel network with low velocity (venules/veins)). For the AG-9 group, T_2 values were lower at week 2 (**figure S2**), while they were significant higher at week 4 (*****p<0.0286), indicative of higher water content at week 4 (**Fig. 5c-d**). Furthermore, ADC values indicate a dense tumor mass (lower ADC values) at early time points (**Fig. 5e-f**, **figure S2**). Moreover, homogenous tumors (no macroscopically detectable necrotic regions) were seen in all groups. MRI shows more accurate information compared to optical imaging concerning tumor growth and tissue composition. EDPs directly influenced PDAC cell amount in tumors and AG-9 had the highest effect on tumor growth.

Tumor vascularization and the impact of elastin-derived peptides on angiogenesis.

Tumor vascularization was assessed by 3D MR angiography *in vivo,* showing penetrating patent vessel in tumors (**Fig. 6a-c**). From the MRA, we could identify mature vessels ending in close vicinity of the tumor in all groups. Only in the AG-9 group, these mature vessels are penetrating the tumor in three out of four animals. Interestingly, the only animal in which we could not detect penetrating mature vessels from MR angiography data is the one with the smallest tumor volume (244.6mm^3 compared to 533-646mm^3 for the tumors in the three other animals) (**Fig. 6d**).

DISCUSSION

For the last three decades, many publications have stressed the important role of different EDPs in influencing cell migration (14), proliferation, chemotaxis (33–35), survival, tumor progression (14,16,36–39), angiogenesis (40), aneurysm formation and atherogenesis (41). VG-6 is, among them, the most frequently described (14,15,34,38,40,42–51). It modulates many physiological and pathological phenomena such as invasiveness ability to form metastases in fibrosarcoma, lung cancer and melanoma, aggressiveness in glioblastoma, angiogenesis, aneurysm formation and atherogenesis (14–16,38,40,51). We previously demonstrated that the xGxxpG consensus sequence stabilizes a type VIII β-turn in several similar, but not identical peptides that maintain a sufficient conformation to be recognized by the elastin receptor complex at the fibroblast cell surface (49). Da Silva *et al* compared AG-9 and VG-6 reference peptides using circular dichroism, nuclear magnetic resonance and Fourier-transform infrared spectroscopy, showing similar structural features (16). They highlighted that xGxPGxGxG peptides, such as AG-9, modulate the same biological activities as xGxxPG but in a more efficient manner. Cell adhesion, proteinase secretion, cell migration, cell proliferation and angiogenesis were systematically more pronounced under AG-9 conditions compared to VG-6 conditions. The RPSA receptor was identified with AG-9 or VG-6 affinity chromatography (16). AG-9 induced cancer cell blebbing and shedding of extracellular vesicles through RPSA binding (38). A public database search was first performed in this study, demonstrating the presence of RPSA in almost all human tissue types. In pancreatic tissue, RPSA is present under normal and pathological conditions. In pancreatic cancer, RPSA is a marker for poor prognosis (21,32). Furthermore, pancreatic elastases promote the release of EDPs in pancreas (12). EDPs interact directly with RPSA and initiate or further promote cancer progression. In case of EDP diffusion, this also occurs far from the pancreas, potentially promoting formation of metastases (52,53). In this study, we focused on a murine xenograft model of pancreatic cancer using MIA PaCa-2 cells, a PDAC cell line in which we already demonstrated the high expression of RPSA (21). PDAC is characterized by an abundant and intense desmoplastic stroma, originating from a fibrotic response of healthy tissue to invasive carcinoma by an abnormal accumulation of ECM components and cell landscape which correspond to 90% with the tumor mass (54). Desmoplastic stroma leads to modifications in the local immune system and vascularization, hereby influencing

prognosis (55). *In vivo* PDAC models are mainly represented by genetically engineered mouse models of the KRAS (for Kristen RAS) proto-oncogene (56). KRAS is a small GTPase of the RAS family and is involved in several signaling pathways leading to cell proliferation (57). The proto-oncogene is found is more than 90% of PDACs. A correlation with poor prognosis has been reported (58). Furthermore, an accumulation of hyaluronan was observed in tumor stroma, which leads to reduced elasticity of tumor tissue, a high interstitial fluid pressure blocking and reduced distribution of therapeutic agents (59). To our knowledge, the role of EDPs in PDAC *in vivo* has not yet been described. The most frequently used *in vivo* PDAC model is the MIA PaCa-2 cell line xenograft (60). We aimed at using multi-modal imaging to better characterize our model longitudinally. We demonstrated that we efficiently transduced our cell line for the expression of eGFP and FLuc with preservation of the expression of RPSA, a pre-requisite in our study.

Our data clearly indicate that EDPs, especially AG-9, are associated with rapidly growing pancreatic allografts. MIA PaCa-2/eGFP-FLuc$^+$ xenografts showed an increase of tumor growth under the influence of EDPs while preserving their relatively homogenous composition as determined by MRI. This finding is in line with results from other groups that have reported on the influence of EDP in other cancer types such as sarcoma and lung tumor (14,15,38). Interestingly, VG-6 was previously tested as a reference peptide in terms of cancer progression (16). In our study, VG-6 has only a small effect on pancreatic tumor growth, compared to AG-9, which doubles the size of tumors compared to the control group. Hereby, multimodal/multiparametric imaging provides not only information on tumor size changes as an effect of EDP on PDAC development in a mouse model but also other structural and functional information. This includes longitudinal information on cell viability, cell density, expression of target-genes by preclinical optical imaging, tumor tissue heterogeneity/homogeneity and tumor vascularization using MRI (T_2 and ADC maps). From our *ex vivo* studies of tumor volume and mass (**Fig. 3**), we estimated the tumor density which slightly decreased over time in both AG-9 and VG-6 groups. This is also confirmed by a non-significant decrease in ADC values from diffusion MRI and by optical imaging data. The quantitative MRI assessment (parametric T_2 and ADC maps) show values similar to what was reported in the literature for this model (61,62). The only significant change we have observed was an increase of T_2 values over time for the AG-9 group, which could reflect subtle structural remodeling such as an increase of vascularization, which was also observed in the MR angiography experiments. We hypothesized that such changes in vascularization could also influence tumor metabolism. In a recent publication small metabolic and topologic differences were reported between MIA PaCa-2 and Hs 766-T tumors, another model of pancreatic tumour (63). Our results also confirm a previous hypothesis on hypervascularization of MIA PaCa-2 tumors (62,64).

Non-invasive longitudinal multimodal imaging enables the follow-up of the same animal during the disease progression, increasing the statistical power and giving more information with the same number of animals (65). Preclinical MRI is a potentially multiparametric technique, which offers numerous

outcome measures during a single MRI session and is in line with the 3R principle. In combination with other imaging modalities (i.e., PET or optical imaging) and complementing with clinical examinations and histological validation, a refinement of animals is performed and the reduction in animal numbers is accomplished. We designed the experiment with five mice per group, according to the G-power calculation and to the European guidelines (3R rule). AG-9 significantly increased tumor growth. Unfortunately, one graft did not grow in the AG-9 group and two mice died (control and VG-6 groups) just before the acquisitions at 28th day). Although, by increasing the sample size will probably resulted in a significant increase of tumor sizes for the VG-6 group, we demonstrated the more potent effect of AG-9 which was the main objective of this study.

For ex-vivo experiments, histological validations were performed to confirm the expression and localization of markers (GFP, FLuc and RPSA). To date, several technologies are available to analyze proteins in a tissue specimen. Along with or in addition to histology, mass spectroscopy offers many advantages. Matrix-assisted laser desorption/ionization (MALDI) imaging mass spectrometry (IMS) analysis of tissue is a technology that can be used to assess the localization of proteins (66). However, gas-phase fragmentation efficiency of MALDI generated proteins presents significant challenges, making macromolecules identification directly from tissue difficult (67). For future ex-vivo experiments, MALDI-IMS will be considered to determine the spatial distributions of many peptides and proteins from tissue sections. This approach will allow us to study changes in expression levels and protein distributions associated with PDAC development. »

To conclude, the present study highlights the AG-9 pro-tumor effect *in vivo*, which we have previously reported to stimulate migration in MIA PaCa-2 cells *in vitro*. Moreover, our findings are of interest for studies in pancreatic cancer, especially to test pro-oncogenic or anti-oncogenic molecules and/or drugs. Subcutaneous xenografts of human-derived cell lines in immunodeficient animals are the most frequently used models in preclinical cancer research. This model has several advantages, including technical feasibility and tumor accessibility (direct measurement of the subcutaneous tumor allowing longitudinal follow up as well as easy BLI and FLI measurement). In term of stroma reaction, Bhardwaj *et al,* and Wegner *et al*, showed an ECM enrichment (collagen I, collagen IV and fibronectin) in orthotopic and subcutaneous MIA PaCa-2 models, respectively (68,69). However, recent studies on tumor stroma involvement in drug resistance, metastasis formation, immune escape and angiogenesis strongly suggests that orthotopic models should provide valuable information that one could not obtain from sub-cutaneous models, tumor development in its 'natural' environment. This represents the next step for testing the AG-9 peptide *in vivo*. We will also consider highly metastatic tumors with abundant elastin tissue such as lungs or liver carcinoma.

AUTHOR CONTRIBUTIONS:

L.N, W.G, U.H, C.G, J.W, S.B and B.B designed, performed, and analyzed all the experiments. L.N wrote the paper with B.B, W.G, U.H and S.B.P. provided essential editorial oversight and critical review.

ACKNOWLEDGMENTS

This work was supported by grants from the European Commission for the PANA project (H2020-NMP-2015-two-stage, grant 686009), the Centre National de la Recherche Scientifique (UMR7369), the University of Reims Champagne-Ardenne, the Region Champagne-Ardenne and the Department Imaging and Pathology of KU Leuven provided a FLOV mandate to partially finance LNs PhD scholarship. The authors gratefully acknowledge the VIB Bio Imaging Core of KU Leuven for their support and assistance in this work. The authors thank the PICT-IBiSA Platform of the University of Reims Champagne-Ardenne (France), Dr. Carla Rios Luci and Pr. Stefaan Soenen (NanoHealth and Optical Imaging Group, KU Leuven, Belgium), Dr. Bella Manshian (Translational Cell and Tissue Research, KU Leuven, Belgium) and Aurélie Dupont-Deshorgue (UMR7369) for their skillful technical assistance.

Conflict of Interest statement:

The authors declare no conflict of interest.

Data availability statement:

The data that support the findings of this study are available from the corresponding author upon reasonable request.

Ethics approvals statement:

This manuscript does not need any ethics approval.

Patient consent statement:

This manuscript does not contain any individual person’s data.

REFERENCES

1. Rahib L, Smith BD, Aizenberg R, Rosenzweig AB, Fleshman JM, Matrisian LM. Projecting cancer incidence and deaths to 2030: the unexpected burden of thyroid, liver, and pancreas cancers in the United States. Cancer Res . 2014 Jun ;74(11):2913–21.

2. Kamisawa T, Wood LD, Itoi T, Takaori K. Pancreatic cancer. Lancet (London, England) . 2016

Jul 2 ;388(10039):73–85.

3. Rawla P, Sunkara T, Gaduputi V. Epidemiology of Pancreatic Cancer: Global Trends, Etiology and Risk Factors. World J Oncol . 2019;10(1):10–27.

4. Procacci P, Moscheni C, Sartori P, Sommariva M, Gagliano N. Tumor–Stroma Cross-Talk in Human Pancreatic Ductal Adenocarcinoma: A Focus on the Effect of the Extracellular Matrix on Tumor Cell Phenotype and Invasive Potential. Cells . 2018 Oct 5 ;7(10):1. – 12 of 12.

5. Feig C, Gopinathan A, Neesse A, Chan DS, Cook N, Tuveson DA. The pancreas cancer microenvironment. Clin Cancer Res . 2012 Aug 15;18(16):4266–76.

6. Thomas D, Radhakrishnan P. Tumor-stromal crosstalk in pancreatic cancer and tissue fibrosis. Mol Cancer . 2019 Jan 21;;18(1):14.

7. Shapiro SD, Endicott SK, Province MA, Pierce JA, Campbell EJ. Marked longevity of human lung parenchymal elastic fibers deduced from prevalence of D-aspartate and nuclear weapons-related radiocarbon. J Clin Invest . 1991;87(5):1828–34.

8. Qin Z. Soluble elastin peptides in cardiovascular homeostasis: Foe or ally. Peptides . 2015 May 1;67:64–73.

9. Quan T, Wang F, Shao Y, Rittié L, Xia W, Orringer JS, et al. Enhancing structural support of the dermal microenvironment activates fibroblasts, endothelial cells, and keratinocytes in aged human skin in vivo. J Invest Dermatol . 2013;133(3):658–67.

10. Robert L, Robert AM, Jacotot B. Elastin-elastase-atherosclerosis revisited . Vol. 140, Atherosclerosis. Atherosclerosis; 1998. p. 281–95.

11. Sellami M, Meghraoui-Kheddar A, Terryn C, Fichel C, Bouland N, Diebold MD, et al. Induction and regulation of murine emphysema by elastin peptides. Am J Physiol - Lung Cell Mol Physiol . 2016 Jan 1;310(1):L8–23.

12. Baló J, Banga I. Elastase and elastase-inhibitor. Nature . 1949 ;164(4168):491.

13. Maquart FX, Pasco S, Ramont L, Hornebeck W, Monboisse JC. An introduction to matrikines: Extracellular matrix-derived peptides which regulate cell activity - Implication in tumor invasion. Critical Reviews in Oncology/Hematology. 2004. 49(3):199-202.

14. Donet M, Brassart-Pasco S, Salesse S, Maquart FX, Brassart B. Elastin peptides regulate HT-1080 fibrosarcoma cell migration and invasion through an Hsp90-dependent mechanism. Br J Cancer. 2014; 111(1):139-48.

15. Toupance S, Brassart B, Rabenoelina F, Ghoneim C, Vallar L, Polette M, et al. Elastin-derived

peptides increase invasive capacities of lung cancer cells by post-transcriptional regulation of MMP-2 and uPA. Clin Exp Metastasis. 2012; 29(5):511-22.

16. Da Silva J, Lameiras P, Beljebbar A, Berquand A, Villemin M, Ramont L, et al. Structural characterization and in vivo pro-tumor properties of a highly conserved matrikine. Oncotarget . 2018 Apr 1;9(25):17839–57.

17. Castronovo V, Claysmith AP, Barker KT, Cioce V, Krutzsch HC, Sobel ME. Biosynthesis of the 67 kDa high affinity laminin receptor. Biochem Biophys Res Commun . 1991 May 31;177(1):177–83.

18. Digiacomo V, Meruelo D. Looking into laminin receptor: Critical discussion regarding the non-integrin 37/67-kDa laminin receptor/RPSA protein. Biol Rev. 2016; 91(2):288-310.

19. Mecham RP, Hinek A, Griffin GL, Senior RM, Liotta LA. The elastin receptor shows structural and functional similarities to the 67-kDa tumor cell laminin receptor. J Biol Chem. 1989;264(28):16652–7.

20. Mercurio AM. Laminin receptors: achieving specificity through cooperation. Vol. 5, Trends in Cell Biology. 1995. p. 419–23.

21. Lefebvre T, Rybarczyk P, Bretaudeau C, Vanlaeys A, Cousin R, Brassart-Pasco S, et al. TRPM7/RPSA Complex Regulates Pancreatic Cancer Cell Migration. Front Cell Dev Biol . 2020 Jul 8; 8:549.

22. Treadwell JR, Zafar HM, Mitchell MD, Tipton K, Teitelbaum U, Jue J. Imaging Tests for the Diagnosis and Staging of Pancreatic Adenocarcinoma: A Meta-Analysis. Pancreas . 2016 Jul 1;45(6):789–95.

23. Tamm EP, Balachandran A, Bhosale PR, Katz MH, Fleming JB, Lee JH, et al. Imaging of pancreatic adenocarcinoma: update on staging/resectability. Radiol Clin North Am . 2012 May;50(3):407–28.

24. Hee SP, Jeong ML, Hei KC, Sung HH, Joon KH, Byung IC. Preoperative evaluation of pancreatic cancer: comparison of gadolinium-enhanced dynamic MRI with MR cholangiopancreatography versus MDCT. J Magn Reson Imaging . 2009 Sep ;30(3):586–95.

25. Wang Y, Miller FH, Chen ZE, Merrick L, Mortele KJ, Hoff FL, et al. Diffusion-weighted MR imaging of solid and cystic lesions of the pancreas. Radiographics . 2011 May ; 31(3):E47-64.

26. Mitchell RA, Stanger D, Shuster C, Telford J, Lam E, Enns R. Repeat Endoscopic Ultrasound-Guided Fine-Needle Aspiration in Patients with Suspected Pancreatic Cancer: Diagnostic Yield and Associated Change in Access to Appropriate Care. Can J Gastroenterol Hepatol . 2016;

2016:7678403.

27. Contag CH, Spilman SD, Contag PR, Oshiro M, Eames B, Dennery P, et al. Visualizing Gene Expression in Living Mammals Using a Bioluminescent Reporter. Photochem Photobiol . 1997;66(4):523–31.

28. Hilderbrand SA, Weissleder R. Near-infrared fluorescence: application to in vivo molecular imaging. Curr Opin Chem Biol . 2010 Feb;14(1):71–9.

29. Koh DM, Collins DJ. Diffusion-weighted MRI in the body: Applications and challenges in oncology. Am J Roentgenol . 2007 Jun;188(6):1622–35.

30. Koh DM, Padhani AR. Diffussion-weighted MRI: A new functional clinical technique for tumour imaging . Vol. 79, British Journal of Radiology. Br J Radiol; 2006 . p. 633–5.

31. Leten C, Roobrouck VD, Struys T, Burns TC, Dresselaers T, Vande Velde G, et al. Controlling and monitoring stem cell safety in vivo in an experimental rodent model. Stem Cells . 2014 Nov 1;32(11):2833–44.

32. Wu Y, Tan X, Liu P, Yang Y, Huang Y, Liu X, et al. ITGA6 and RPSA synergistically promote pancreatic cancer invasion and metastasis via PI3K and MAPK signaling pathways. Exp Cell Res . 2019 Jun 1;379(1):30–47.

33. Long MM, King VJ, Prasad KU, Urry DW. Chemotaxis of fibroblasts toward nonapeptide of elastin. BBA - Mol Cell Res. 1988;968(3):300–11.

34. Senior RM, Griffin GL, Mecham RP, Wrenn DS, Prasad KU, Urry DW. Val-Gly-Val-Ala-Pro-Gly, a repeating peptide in elastin, is chemotactic for fibroblasts and monocytes. J Cell Biol. 1984;99(3):870–4.

35. Mochizuki S, Brassart B, Hinek A. Signaling pathways transduced through the elastin receptor facilitate proliferation of arterial smooth muscle cells. J Biol Chem. 2002; 277(47):44854-63.

36. Huet E, Brassart B, Cauchard JH, Debelle L, Birembaut P, Wallach J, et al. Cumulative influence of elastin peptides and plasminogen on matrix metalloproteinase activation and type I collagen invasion by HT-1080 fibrosarcoma cells. Clin Exp Metastasis. 2002; 19(2):107-17.

37. Brassart B, Randoux A, Hornebeck W, Emonard H. Regulation of matrix metalloproteinase-2 (gelatinase A, MMP-2), membrane-type matrix metalloproteinase-1 (MT1-MMP) and tissue inhibitor of metalloproteinases-2 (TIMP-2) expression by elastin-derived peptides in human HT-1080 fibrosarcoma cell line. Clin Exp Metastasis . 1998;16(6):489–500.

38. Brassart B, Da Silva J, Donet M, Seurat E, Hague F, Terryn C, et al. Tumour cell blebbing and extracellular vesicle shedding: key role of matrikines and ribosomal protein SA. Br J Cancer.

2019 Feb 19;120(4):453–65.

39. Ntayi C, Labrousse AL, Debret R, Birembaut P, Bellon G, Antonicelli F, et al. Elastin-Derived Peptides Upregulate Matrix Metalloproteinase-2-ediated Melanoma Cell Invasion Through Elastin-Binding Protein. J Invest Dermatol. 2004; 122(2):256-65.

40. Robinet A, Fahem A, Cauchard JH, Huet E, Vincent L, Lorimier S, et al. Elastin-derived peptides enhance angiogenesis by promoting endothelial cell migration and tubulogenesis through upregulation of MT1-MMP . Vol. 118, Journal of Cell Science. J Cell Sci; 2005. p. 343–56.

41. Dale MA, Xiong W, Carson JS, Suh MK, Karpisek AD, Meisinger TM, et al. Elastin-Derived Peptides Promote Abdominal Aortic Aneurysm Formation by Modulating M1/M2 Macrophage Polarization. J Immunol . 2016;196(11):4536–43.

42. Hance KA, Tataria M, Ziporin SJ, Lee JK, Thompson RW. Monocyte chemotactic activity in human abdominal aortic aneurysms: role of elastin degradation peptides and the 67-kD cell surface elastin receptor. J Vasc Surg Off Publ Soc Vasc Surg Int Soc Cardiovasc Surg North Am Chapter. 2002;35:254–61.

43. Huet E, Brassart B, Wallach J, Debelle L, Haye B, Emonard H, et al. Effect of elastin peptides on the production of matrix metalloproteinase 2 by human skin fibroblasts in culture. J Soc Biol . 2001;195(2):165–72.

44. Brassart B, Fuchs P, Huet E, Alix AJP, Wallach J, Tamburro AM, et al. Conformational Dependence of Collagenase (Matrix Metalloproteinase-1) Up-regulation by Elastin Peptides in Cultured Fibroblasts. J Biol Chem. 2001; 276(7):5222-7.

45. Hinek A, Boyle J, Rabinovitch M. Vascular smooth muscle cell detachment from elastin and migration through elastic laminae is promoted by chondroitin sulfate-induced “shedding” of the 67-kDa cell surface elastin binding protein. Exp Cell Res. 1992;203:344–53.

46. Coquerel B, Poyer F, Torossian F, Dulong V, Bellon G, Dubus I, et al. Elastin-derived peptides: Matrikines critical for glioblastoma cell aggressiveness in a 3-D system. Glia . 2009;57(16):1716–26.

47. Fahem A, Robinet A, Cauchard JH, Duca L, Soula-Rothhut M, Rothhut B, et al. Elastokine-mediated up-regulation of MT1-MMP is triggered by nitric oxide in endothelial cells. Int J Biochem Cell Biol. 2008; 40(8):1581-96.

48. Nackman GB, Karkowski FJ, Halpern VJ, Gaetz HP, Tilson MD. Elastin degradation products induce adventitial angiogenesis in the Anidjar/Dobrin rat aneurysm model. Surgery . 1997;122(1):39–44.

49. Debret R, Le Naour RR, Sallenave JM, Deshorgue A, Hornebeck WG, Guenounou M, et al. Elastin fragments induce IL-1β upregulation via NF-κB pathway in melanoma cells. J Invest Dermatol. 2006; 126(8):1860-8.

50. Szychowski KA, Gmiński J. Impact of elastin-derived VGVAPG peptide on bidirectional interaction between peroxisome proliferator-activated receptor gamma (Pparγ) and beta-galactosidase (β-Gal) expression in mouse cortical astrocytes in vitro. Naunyn Schmiedebergs Arch Pharmacol . 2019 Apr 2 ;392(4):405–13.

51. Pocza P, Süli-Vargha H, Darvas Z, Falus A. Locally generated VGVAPG and VAPG elastin-derived peptides amplify melanoma invasion via the galectin-3 receptor. Int J Cancer. 2008; 122(9):1972-80.

52. Timár J, Diczházi C, Ladányi A, Rásó E, Hornebeck W, Robert L, et al. Interaction of tumour cells with elastin and the metastatic phenotype. Ciba Found Symp . 1995 ; 192:321-35.

53. Yusa T, Blood CH, Zetter BR. Tumor cell interactions with elastin: implications for pulmonary metastasis. Am Rev Respir Dis . 1989;140(5):1458–62.

54. Liot S, Balas J, Aubert A, Prigent L, Mercier-Gouy P, Verrier B, et al. Stroma Involvement in Pancreatic Ductal Adenocarcinoma: An Overview Focusing on Extracellular Matrix Proteins. Front Immunol . 2021 Apr 6; 12:612271.

55. Li KY, Yuan JL, Trafton D, Wang JX, Niu N, Yuan CH, et al. Pancreatic ductal adenocarcinoma immune microenvironment and immunotherapy prospects. Chronic Dis Transl Med . 2020 Mar 1;6(1):6–17.

56. Vasseur R, Skrypek N, Duchêne B, Renaud F, Martínez-Maqueda D, Vincent A, et al. The mucin MUC4 is a transcriptional and post-transcriptional target of K-ras oncogene in pancreatic cancer. Implication of MAPK/AP-1, NF-κB and RalB signaling pathways. Biochim Biophys Acta . 2015 Dec 1;1849(12):1375–84.

57. Timar J, Kashofer K. Molecular epidemiology and diagnostics of KRAS mutations in human cancer. Cancer Metastasis Rev . 2020 Dec 1;39(4):1029–38.

58. Buscail L, Bournet B, Cordelier P. Role of oncogenic KRAS in the diagnosis, prognosis and treatment of pancreatic cancer. Nat Rev Gastroenterol Hepatol . 2020 Mar 1 ;17(3):153–68.

59. Sato N, Cheng XB, Kohi S, Koga A, Hirata K. Targeting hyaluronan for the treatment of pancreatic ductal adenocarcinoma. Acta Pharm Sin B . 2016 Mar 1 ;6(2):101–5. 92/

60. Delaney LJ, Eisenbrey JR, Brown D, Brody JR, Jimbo M, Oeffinger BE, et al. Gemcitabine-loaded microbubble system for ultrasound imaging and therapy. Acta Biomater . 2021 Aug 1

;130:385–94.

61. Kobes JE, Daryaei I, Howison CM, Bontrager JG, Sirianni RW, Meuillet EJ, et al. Improved Treatment of Pancreatic Cancer With Drug Delivery Nanoparticles Loaded With a Novel AKT/PDK1 Inhibitor. Pancreas . 2016 Sep 1;45(8):1158–66.

62. Zhang X, Wojtkowiak JW, Martinez G V., Cornnell HH, Hart CP, Baker AF, et al. MR Imaging Biomarkers to Monitor Early Response to Hypoxia-Activated Prodrug TH-302 in Pancreatic Cancer Xenografts. PLoS One . 2016 May 1; 11(5):e0155289.

63. Kishimoto S, Brender JR, Crooks DR, Matsumoto S, Seki T, Oshima N, et al. Imaging of glucose metabolism by 13C-MRI distinguishes pancreatic cancer subtypes in mice. Elife . 2019 Aug 1; 8:e46312.

64. Kim H, Rigell CJ, Zhai G, Lee SK, Samuel SL, Martin A, et al. Antagonistic effects of anti-EMMPRIN antibody when combined with chemotherapy against hypovascular pancreatic cancers. Mol imaging Biol . 2014 Feb;16(1):85–94.

65. Wachsmuth L, Mensen A, Barca C, Wiart M, Tristão-Pereira C, Busato A, et al. Contribution of preclinical MRI to responsible animal research: living up to the 3R principle. Magn. Reson. Mat. Phys. Biol. Med. 2021 Aug 1;34(4):469–74.

66. Kubo A, Kajimura M, Suematsu M. Matrix-Assisted Laser Desorption/Ionization (MALDI) Imaging Mass Spectrometry (IMS): A Challenge for Reliable Quantitative Analyses. Mass Spectrom (Tokyo, Japan). 2012;1(1):A0004–A0004.

67. Ryan DJ, Spraggins JM, Caprioli RM. Protein identification strategies in MALDI imaging mass spectrometry: a brief review. Curr Opin Chem Biol. 2019 Feb 1;48:64–72.

68. Bhardwaj A, Srivastava SK, Singh S, Tyagi N, Arora S, Carter JE, et al. MYB Promotes Desmoplasia in Pancreatic Cancer through Direct Transcriptional Up-regulation and Cooperative Action of Sonic Hedgehog and Adrenomedullin. J Biol Chem. 2016, 291(31):16263–70.

69. Wegner CS, Gaustad JV, Andersen LMK, Simonsen TG, Rofstad EK. Diffusion-weighted and dynamic contrast-enhanced MRI of pancreatic adenocarcinoma xenografts: associations with tumor differentiation and collagen content. J Transl Med. 2016 Jun 7 ;14(1).

FIGURE TITLES AND LEGENDS:

Fig. 1: RPSA expression in healthy and pancreatic tissue. a. Protein expression of RPSA in human tissues from the Human Protein Atlas cohort. **b.** RNA expression of RPSA in human tissues. Consensus Normalized Expression (NX) levels by combining the data from different transcriptomics datasets

(HPA, GTEx and FANTOM5) using the internal normalization pipeline of the Human Protein Atlas. **c.** Microphotographs of RPSA IHC in normal and pancreatic carcinoma tissue microarrays from the Human Protein Atlas dataset. Anti-RPSA pAb (sc-20979, Santa Cruz Biotechnology) has been used at a 1:100 dilution for IHC staining. **d.** Distribution of pancreatic cancer cases among four levels of RPSA staining intensity (*Blue*) and fraction of cells stained (*Brown*) from the Human Protein Atlas dataset.

Fig. 2: Generation of stable reporter gene expression in the pancreatic cancer cell line for optical imaging. a. Schematic representation of the eGFP-FLuc$^+$ lentiviral vector used for MIA PaCa-2/WT transduction. **b.** Representative *in vitro* BLI of WT and transduced MIA PaCa-2 cells. **c.** Box plot and whiskers quantification of total photon flux (p/sec) of BLI signal intensities *in vitro* (Min to Max, $n = 4$ per group). **d.** Representative *in vitro* FLI of WT and transduced MIA PaCa-2 cells. **e.** Box plot and whiskers quantification of total photon flux (p/sec) of FLI signal intensities *in vitro* (Min to Max, $n = 4$ per group). **f.** Western blot analysis on total proteins extracted from WT and transduced MIA PaCa-2 cells of FLuc and GFP proteins in WT and transduced MIA PaCa-2 cells. The actin antibody was used as internal control. **g.** Total RNAs were purified from WT and transduced MIA PaCa-2 cells. The mRNA level of RPSA was assessed by qPCR. EFa1 mRNA was used for the quantification. **h.** RPSA and TAMRA-EDPs (AG-9 and VG-6) distribution on MIA PaCa-2/eGFP-FLuc$^+$ cells were studied by confocal microscopy. Colocalizations were studied using the 'Colocalization' plugin of ImageJ. Scale bar: 10 µm. Statistical analyses were performed using a *Mann-Whitney* test. The results were considered statistically significant ***** $p<0.05$.

Fig. 3: Evaluation of the elastin-derived peptide on tumor growth in a pancreatic mouse model. a. Mice body weights (BW) post tumor challenge (mean ± standard error of the mean (SEM), Control $n = 5$, AG-9 $n = 4$ and VG-6 $n = 5$). **b.** Tumor volumes post tumor challenge (mm^3) (mean ± SD). **c.** Box plot and whiskers representation of individual tumor volumes on day 28 (mm^3) (Min to Max, Control $n = 5$, AG-9 $n = 4$ and VG-6 $n = 5$). **d.** Box plot and whiskers representation of individual tumor weights on day 28 (Min to Max, Control $n = 5$, AG-9 $n = 4$ and VG-6 $n = 5$). **e.** Representative photographs of MIA PaCa-2/eGFP-FLuc$^+$ xenografts after tumor excision (scale bar: 1 cm). **f.** S.c. xenograft whole sections stained with HE. **g.** IHC analyses of s.c. PDAC xenograft whole sections allowing visualization of RPSA within tumors. All acquisitions were performed with a 20x magnification. Scale bar: 150 mm. Statistical analyses were performed using a *Mann-Whitney* test. The results were considered statistically significant when we compared control to AG-9; *****$p<0.05$, ****** $p<0.01$, AG-9 to VG-6 EDPs; **$** $p<0.05$ and control to VG-6; **#** $p<0.05$.

Fig. 4: Optical imaging approach enables *in vivo* assessment of the effect of elastin-derived peptide on tumor growth. a. Representative *in vivo* BLI of MIA PaCa-2/eGFP-FLuc$^+$ nude mice 2, 3 and 4 weeks after s.c. injection. **b.** Box plot and whiskers quantification of total photon flux (p/sec) of tumor BLI signals (Min to Max, for *n* values see **figure S1c**). **c.** Representative *in vivo* FLI of MIA PaCa-2/eGFP-FLuc$^+$ nude mice at four weeks after s.c. injection. **d.** Box plot and whiskers quantification of total photon flux (p/sec) of tumor FLI signals (Min to Max, for *n* values see **figure S1c**). **e.** Representative e*x vivo* BLI of MIA PaCa-2/eGFP-FLuc$^+$ excised tumor. **f.** Box plot and whiskers quantification of total photon flux (p/sec) signal from the tumor above mentioned in (**e**) (Min to Max, for *n* values see **figure S1c**). The size of the ROI for *in vivo* BLI and FLI was identical for all animals (5.8 cm²). **g-h.** Histological analyses of s.c. PDAC xenograft whole sections allowing visualization of FLuc (**g**), and GFP (**h**) within tumors. All acquisitions were performed with a 20x magnification. Scale bar: 150 mm. Statistical analyses were performed using a *Mann-Whitney* test. The results were considered statistically significant ***** $p<0.05$.

Fig. 5: Magnetic Resonance Imaging (MRI) based *in vivo* assessment of the effect of elastin-derived peptide on tumor growth. a. Representative *in vivo* MRI of 2D T_2-weighted MRI scans of mice with pancreatic tumor xenografts 2 and 4 weeks after s.c. injection. **b.** Box plot and whiskers of tumor volume measurements (mm³) based on anatomical MRI from (**a**) (Min to Max, for *n* values see **figure S1c**). **c.** Representative *in vivo* MRI of parametric T_2-maps of mice with pancreatic tumors 4 weeks after s.c. injection. **d.** Box and whiskers representation of T_2 values (ms) obtained from (**c**) (Min to Max, for *n* values see **figure S1c**) at week 4. **e.** Representative *in vivo* MRI of parametric ADC-maps of mice with pancreatic tumors 4 weeks after s.c. injection. **f.** Box plot and whiskers representation of ADC values (mm²/s) obtained from (**e**) (Min to Max, for *n* values see **figure S1c**) at week 4. Statistical analyses were performed using a *Mann-Whitney* test. The results were considered statistically significant ***** $p<0.05$.

Fig. 6: 3D MRI angiography for *in vivo* assessment of the effect of elastin-derived peptide on tumor vascularization and tumor growth. a. 3D T_2-weighted RARE of the tumor and (**b**) its corresponding 3D TOF MRA maximum intensity projection with the blue arrow pointing to a penetrating patent vessel. Both 3D volumes are spatially co-registered (**c**) (Overlay of anatomical 3D in greyscale and 3D TOF MRA in hot color) and tumor were segmented (green overlay). **d.** 3D TOF MRA patent arteries (red arrows) reached the vicinity of the tumor (red dashed circle, based on T_2-weighted anatomical MRI) and penetrate inside the tumor in some cases.

Fig. 1

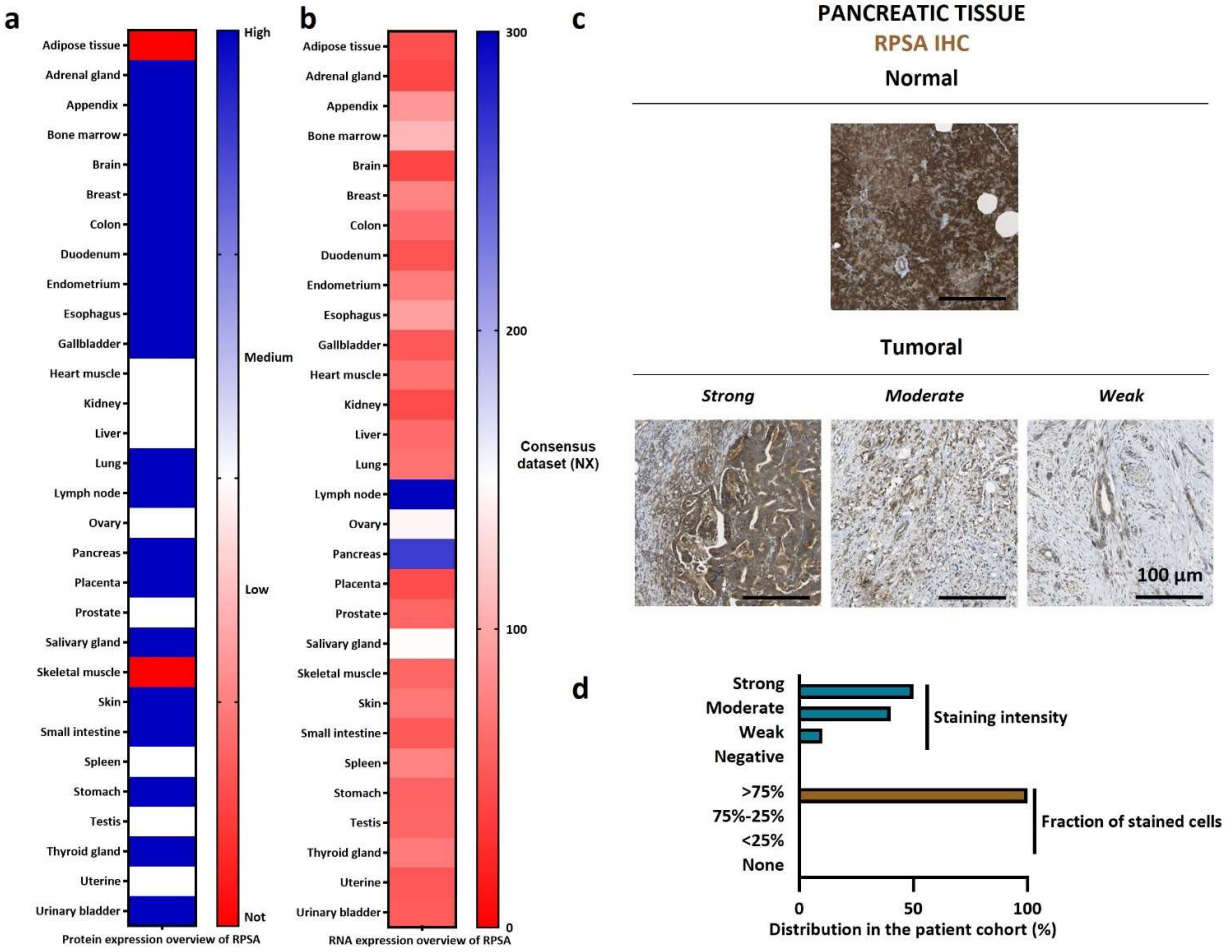
a
b
c
d
Adipose tissue
Adrenal gland
Appendix
Bone marrow
Brain
Breast
Colon
Duodenum
Endometrium
Esophagus
Gallbladder
Heart muscle
Kidney
Liver
Lung
Lymph node
Ovary
Pancreas
Placenta
Prostate
Salivary gland
Skeletal muscle
Skin
Small intestine
Spleen
Stomach
Testis
Thyroid gland
Uterine
Urinary bladder
High
Medium
Low
Not
Protein expression overview of RPSA
300
200
100
0
Consensus dataset (NX)
RNA expression overview of RPSA
PANCREATIC TISSUE
RPSA IHC
Normal
Tumoral
Strong
Moderate
Weak
100 µm
Strong
Moderate
Weak
Negative
Staining intensity
>75%
75%-25%
<25%
None
Fraction of stained cells
0
50
100
Distribution in the patient cohort (%)

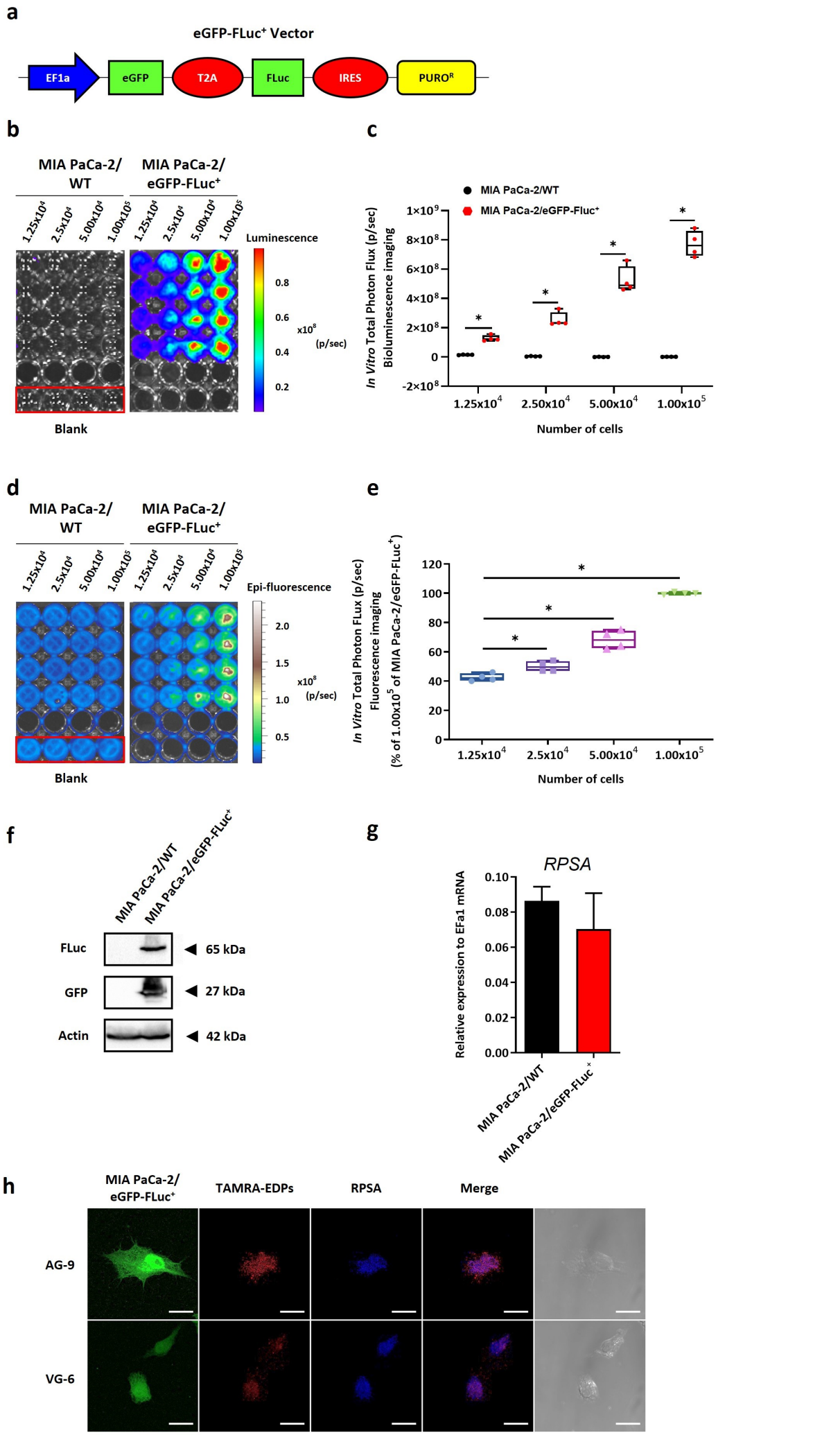
a
eGFP-FLuc+ Vector
EF1a
eGFP
T2A
FLuc
IRES
PURO^R
b
MIA PaCa-2/ WT
MIA PaCa-2/ eGFP-FLuc+
1.25x10^4
2.5x10^4
5.00x10^4
1.00x10^5
Luminescence
0.8
0.6
0.4
0.2
x10^8 (p/sec)
Blank
c
MIA PaCa-2/WT
MIA PaCa-2/eGFP-Fluc+
In Vitro Total Photon Flux (p/sec) Bioluminescence imaging
1x10^9
8x10^8
6x10^8
4x10^8
2x10^8
0
-2x10^8
1.25x10^4
2.50x10^4
5.00x10^4
1.00x10^5
Number of cells
d
MIA PaCa-2/ WT
MIA PaCa-2/ eGFP-FLuc+
Epi-fluorescence
2.0
1.5
1.0
0.5
x10^8 (p/sec)
Blank
e
In Vitro Total Photon FLux (p/sec) Fluorescence imaging (% of 1.00x10^5 of MIA PaCa-2/eGFP-FLuc+)
120
100
80
60
40
20
0
1.25x10^4
2.5x10^4
5.00x10^4
1.00x10^5
Number of cells
f
MIA PaCa-2/WT
MIA PaCa-2/eGFP-FLuc+
FLuc
GFP
Actin
65 kDa
27 kDa
42 kDa
g
RPSA
Relative expression to EFa1 mRNA
0.10
0.08
0.06
0.04
0.02
0.00
MIA PaCa-2/WT
MIA PaCa-2/eGFP-FLuc+
h
MIA PaCa-2/ eGFP-FLuc+
TAMRA-EDPs
RPSA
Merge
AG-9
VG-6

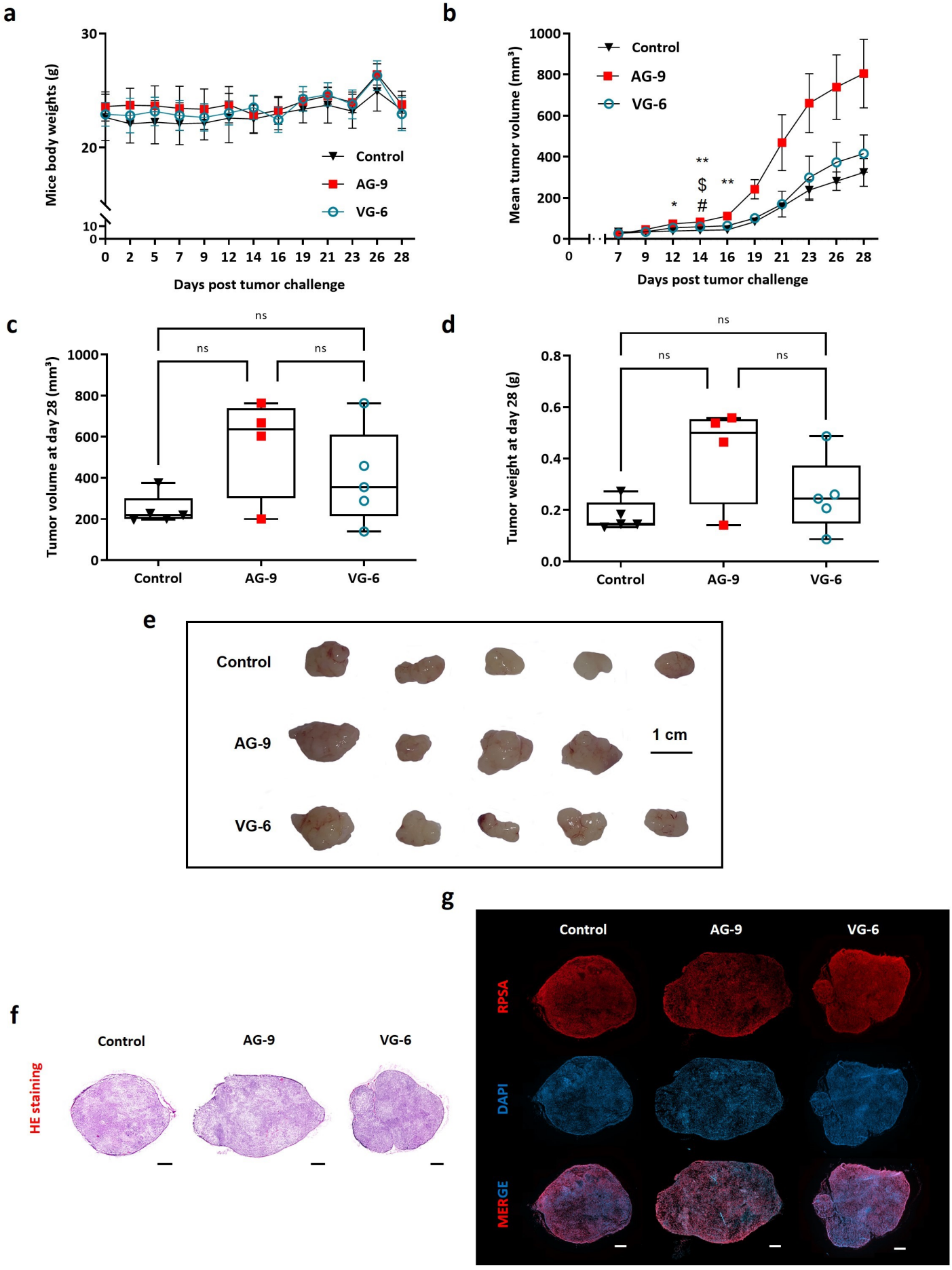
a
Mice body weights (g)
30
20
10
0
0 2 5 7 9 12 14 16 19 21 23 26 28
Days post tumor challenge
Control
AG-9
VG-6
b
Mean tumor volume (mm³)
1000
800
600
400
200
0
0 7 9 12 14 16 19 21 23 26 28
Days post tumor challenge
Control
AG-9
VG-6
*
**
$
#
**
c
Tumor volume at day 28 (mm³)
1000
800
600
400
200
0
ns
ns
ns
Control
AG-9
VG-6
d
Tumor weight at day 28 (g)
0.8
0.6
0.4
0.2
0.0
ns
ns
ns
Control
AG-9
VG-6
e
Control
AG-9
VG-6
1 cm
f
Control
AG-9
VG-6
HE staining
g
Control
AG-9
VG-6
RPSA
DAPI
MERGE

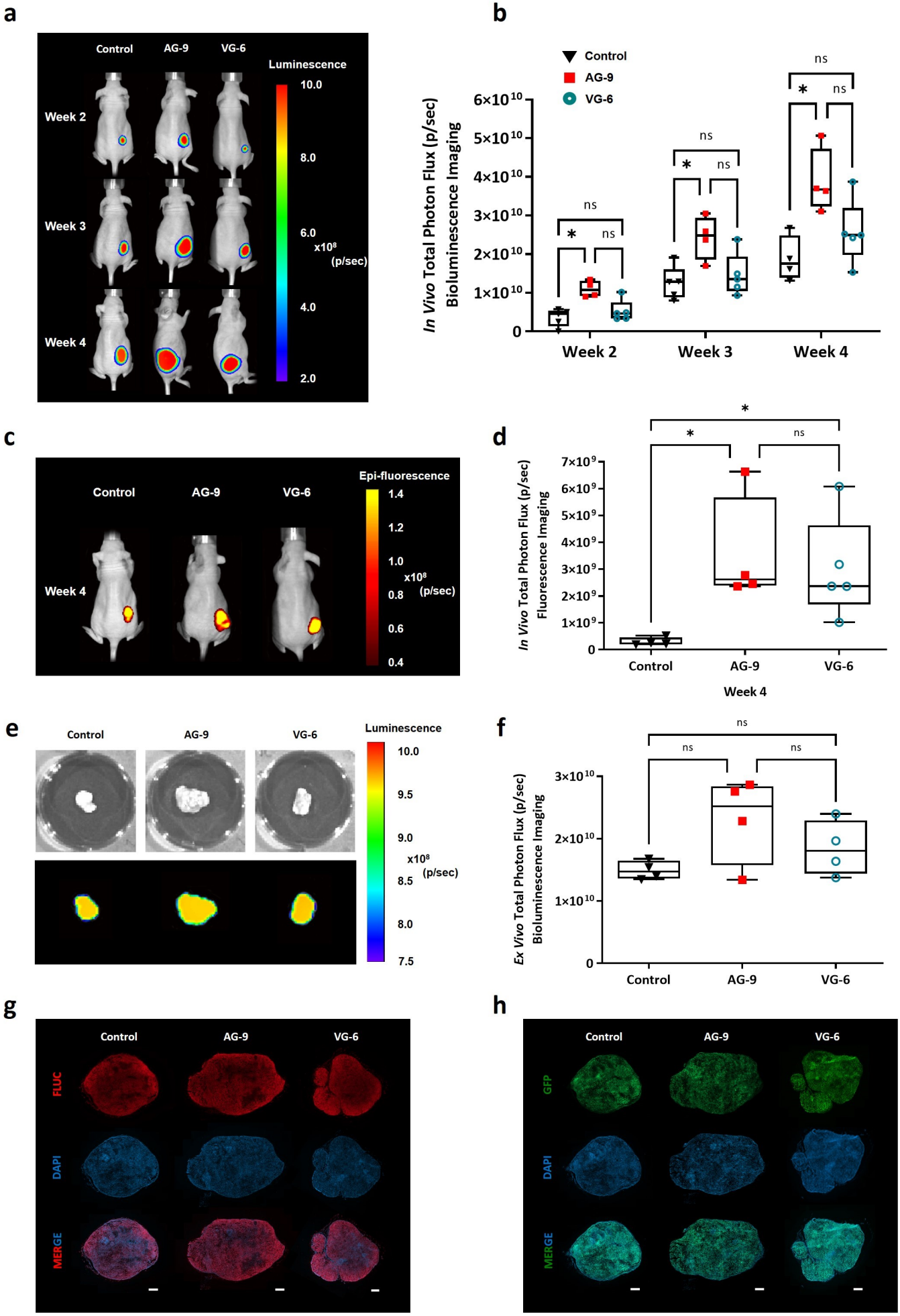
a
Control
AG-9
VG-6
Luminescence
10.0
8.0
6.0
x10⁸
(p/sec)
4.0
2.0
Week 2
Week 3
Week 4
b
Control
AG-9
VG-6
In Vivo Total Photon Flux (p/sec)
Bioluminescence Imaging
6×10¹⁰
5×10¹⁰
4×10¹⁰
3×10¹⁰
2×10¹⁰
1×10¹⁰
0
ns
*
ns
Week 2
Week 3
Week 4
c
Control
AG-9
VG-6
Epi-fluorescence
1.4
1.2
1.0
x10⁸
(p/sec)
0.8
0.6
0.4
Week 4
d
In Vivo Total Photon Flux (p/sec)
Fluorescence Imaging
7×10⁹
6×10⁹
5×10⁹
4×10⁹
3×10⁹
2×10⁹
1×10⁹
0
*
ns
Control
AG-9
VG-6
Week 4
e
Control
AG-9
VG-6
Luminescence
10.0
9.5
9.0
x10⁸
(p/sec)
8.5
8.0
7.5
f
Ex Vivo Total Photon Flux (p/sec)
Bioluminescence Imaging
3×10¹⁰
2×10¹⁰
1×10¹⁰
0
ns
Control
AG-9
VG-6
g
Control
AG-9
VG-6
FLUC
DAPI
MERGE
h
Control
AG-9
VG-6
GFP
DAPI
MERGE

a

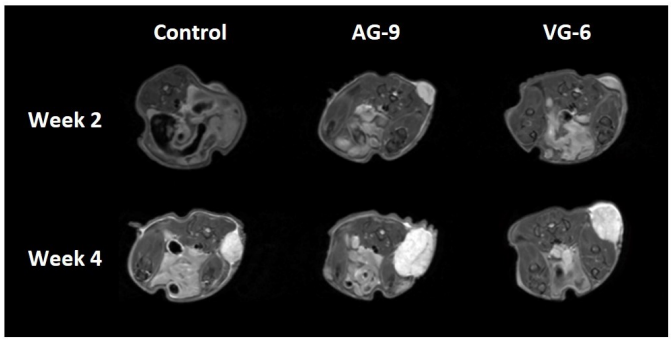
Control
AG-9
VG-6
Week 2
Week 4

b

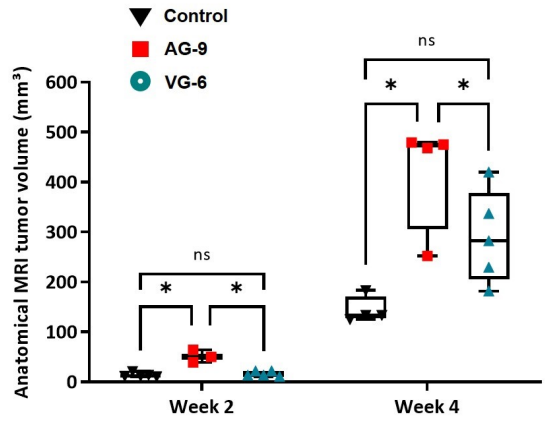
Control
AG-9
VG-6
Anatomical MRI tumor volume (mm³)
600
500
400
300
200
100
0
ns
*
*
ns
*
*
Week 2
Week 4

c

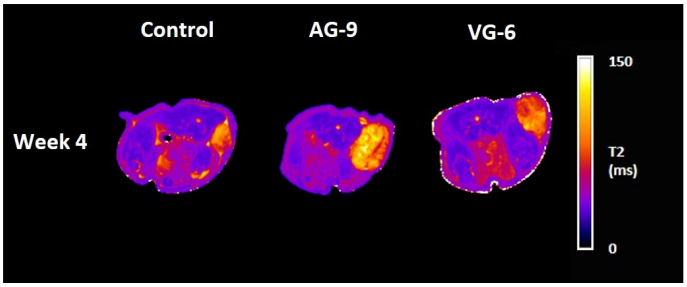
Control
AG-9
VG-6
Week 4
150
T2
(ms)
0

d

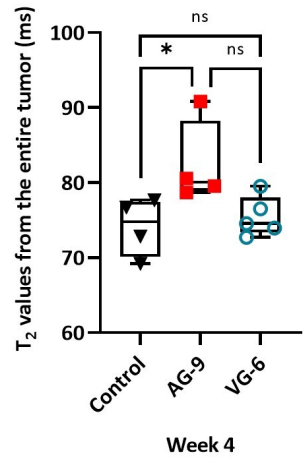
T2 values from the entire tumor (ms)
100
90
80
70
60
ns
*
ns
Control
AG-9
VG-6
Week 4

e

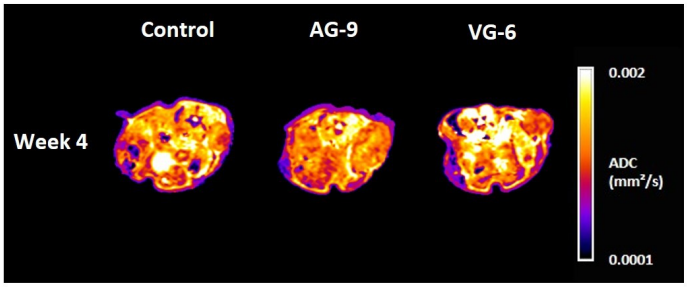
Control
AG-9
VG-6
Week 4
0.002
ADC
(mm²/s)
0.0001

f

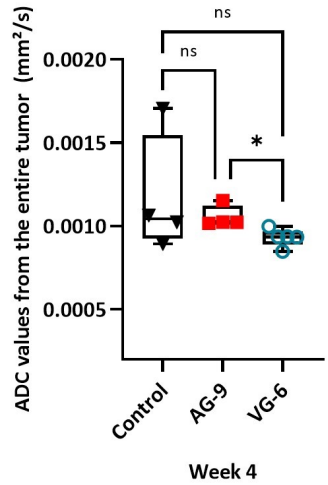
ADC values from the entire tumor (mm²/s)
0.0020
0.0015
0.0010
0.0005
ns
ns
*
Control
AG-9
VG-6
Week 4

Fig. 6:

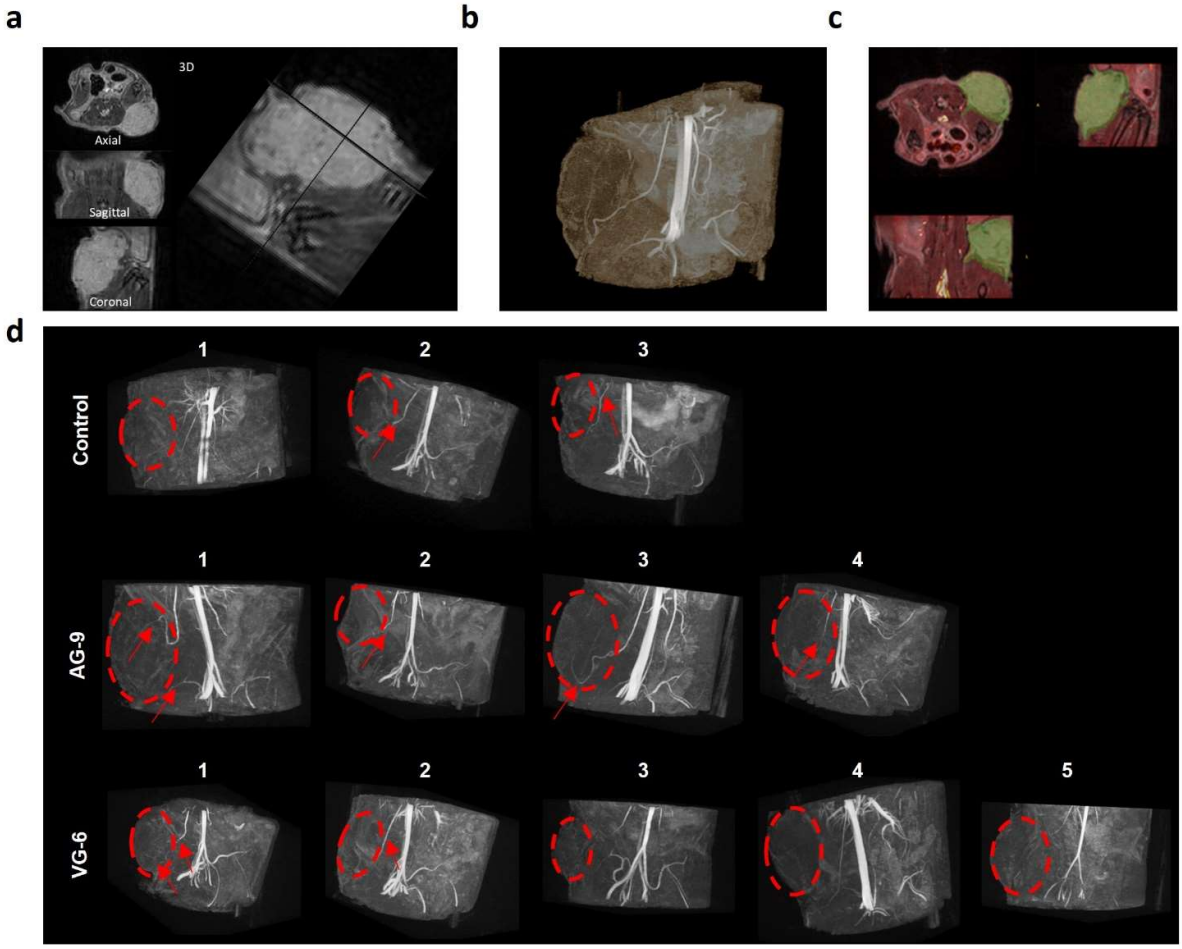
a
b
c
3D
Axial
Sagittal
Coronal
d
Control
1
2
3
AG-9
1
2
3
4
VG-6
1
2
3
4
5